Die Grenzen der Chemie neu ausloten? It takes #HumanChemistry

Wir suchen kreative Chemikerinnen und Chemiker, die mit uns gemeinsam neue Wege gehen wollen – mit Fachwissen, Unternehmertum und Kreativität für innovative Lösungen. Informieren Sie sich unter:

evonik.de/karriere

EVONIK
Leading Beyond Chemistry

ADVANCED FUNCTIONAL MATERIALS
www.afm-journal.de

What Drives the Kinetics and Doping Level in the Electrochemical Reactions of PEDOT:PSS?

*Gonzague Rebetez, Olivier Bardagot, Joël Affolter, Julien Réhault, and Natalie Banerji**

The electrochemical dedoping and redoping processes of a thin poly(3,4-ethylenedioxythiophene):poly(styrenesulfonate) (PEDOT:PSS) film immersed in an electrolyte are studied at different temperatures with time-resolved spectroelectrochemistry in the visible and near-infrared range. The spectral signatures of neutral, polaronic, and bipolaronic states of PEDOT are resolved using multivariate curve resolution analysis. Kinetic modeling of their dynamics reveals that both the dedoping and redoping are sequential processes and occur within a few hundred milliseconds in the system. Evaluation of the temperature-dependence with the Van't Hoff, Arrhenius, and Eyring formalisms highlights the role of entropy in both the establishment of the redox equilibrium at a given voltage bias and the reaction rates. This study provides a significant understanding of the fundamental mechanisms determining the level and rate of the electrochemical processes in PEDOT:PSS and will help tailor the design of faster and more efficient bioelectronic devices based on mixed ionic–electronic conductors.

1. Introduction

Organic mixed ionic–electronic conductors (OMIECs) are materials with the ability to conduct both electronic and ionic charges within their bulk.[1,2] Among these materials, poly(3,4-ethylenedioxythiophene):poly(styrenesulfonate) (PEDOT:PSS) is the most investigated. It is transparent, flexible, very conductive, and benefits from a high biocompatibility and commercial availability, making it a candidate of choice in the field of bioelectronics.[3] A broad panel of top-notch applications ranging from external wearable sensors,[4] in vivo neural activity recording[5] and modulation,[6] to tissue engineering[7] have already emerged.

PEDOT:PSS is composed a positively charged redox active conjugated polymer (PEDOT) mixed with negatively charged insulating PSS. PEDOT:PSS films consist of PEDOT-rich domains surrounded by a spongy PSS-rich matrix.[8–11] Immersed in an aqueous electrolyte solution, the PSS matrix takes up solvated ions and water.[11,12] The electronic transport occurs within the conjugated PEDOT backbone and the ionic transport predominantly in the PSS-rich domains, with ion mobility as high as in water.[8,13] The doping state of PEDOT can be modulated via an external voltage applied between a PEDOT:PSS-coated working electrode and a counter electrode (Ag/AgCl) immersed in an electrolyte. When a negative voltage is applied ($V_{bias} < 0$, dedoping), $PEDOT^{2+}$ (bipolaron) and $PEDOT^{+}$ (polaron) states are reduced to $PEDOT^{+}$ and $PEDOT^{0}$ (neutral) segments, while positively charged ions penetrate the film to compensate the PSS^{-}. Inversely, when a positive voltage is applied ($V_{bias} > 0$), redoping of the film occurs as positively charged ions are expulsed from the film and the PSS^{-} matrix is decompensated by oxidization of $PEDOT^{0}$ and $PEDOT^{+}$ to respectively $PEDOT^{+}$ and $PEDOT^{2+}$.[8–10,14] We note a debate about the nature of $PEDOT^{2+}$, which is sometimes defined as a bipolaron and sometimes as a polaron pair.[14] Resolving this controversy is beyond the scope of our work and the term bipolaron will be used as it is more prominent in the literature.

An imperative step to further develop PEDOT:PSS-based devices is to better understand the fundamental processes occurring between the voltage switch and the change of the electrical properties. The latter depends on the nature and concentration of the charged species (polarons, bipolarons) at a given voltage and can be evaluated using visible-near-infrared (vis–NIR) spectroelectrochemistry.[8–10,14,15] Most reported studies have followed the doping level of organic films by steady-state measurements at different voltages, however such static measurements cannot probe the rate of the dedoping/redoping processes. Recently, the kinetics of anion injection into a glycolated polythiophene film were determined based on the time-resolved (≈100 ms) bleaching of the neutral absorption band.[16] Regarding PEDOT:PSS, first insights to the interconversion of the neutral, polaron, and bipolaron populations upon voltage modulation were obtained with a time-resolution of 0.5 s.[10] The authors focused on the morphological changes occurring during the electrochemical reactions using time-resolved in situ X-ray measurements in combination with spectroelectrochemistry.

Here, we investigate the temperature-dependence of the dedoping/redoping processes in a thin film of PEDOT:PSS

G. Rebetez, O. Bardagot, J. Affolter, J. Réhault, N. Banerji
Department of Chemistry
Biochemistry and Pharmaceutical Sciences
University of Bern
Freiestrasse 3, Bern 3012, Switzerland
E-mail: natalie.banerji@unibe.ch

The ORCID identification number(s) for the author(s) of this article can be found under https://doi.org/10.1002/adfm.202105821.

DOI: 10.1002/adfm.202105821

with a high time-resolution of 5 ms, which allows to access the intrinsic electrochemical redox reactions, which are not limited by the ion dynamics in our experimental conditions. Using a home-built spectroelectrochemical setup and multivariate curve resolution (MCR) analysis, we separate the overlapping spectral signatures of neutral (N), polaronic (P), and bipolaronic (B) states of PEDOT at different voltages and follow their dynamics after the voltage switch. We find that neutral and polaronic species coexist in equilibrium at negative voltage (V_{bias} = –0.6 V), while both polarons and bipolarons are present at slightly positive bias (V_{bias} = +0.1 V). The equilibria evolve with the applied voltage (Nernst-type thermodynamic behavior) and vary with temperature due to the enthalpy and entropy of the reactions (Van't Hoff formalism). From our time-resolved measurements coupled to kinetic modeling, we find that dedoping occurs according to B → P ⇄ N and redoping according to N → P ⇄ B, with both processes being rate limited by the slow establishment of the final equilibrium. The dedoping is driven by enthalpy, while the redoping is driven by entropy. From the temperature-dependent analysis, we also deduce that the reaction rates (activation barriers) are predominantly determined by entropic effects, which are likely related to changes in the backbone conformation and chain packing during the redox reactions. This finding highlights the intrinsic device switching speed that can be achieved in situations where ion diffusion is not the slowest process (for example in PEDOT:PSS-based organic electrochemical transistors, OECTs, with small channels). Furthermore, our experiments and analysis can easily be transferred to other OMIECs, offering a robust and versatile procedure for comparing doping mechanisms between materials.

2. Results

2.1. Steady-State Spectroelectrochemistry

A thin PEDOT:PSS film (4 × 4 mm² × 100 nm) was obtained by spin-coating a PEDOT:PSS solution with ethylene glycol, dodecylbenzene sulfonic acid, and cross-linker additives onto indium tin oxide (ITO) glass (see the Experimental Section). This working electrode was immersed together with an Ag/AgCl reference/counter electrode in a cuvette containing 0.1 M NaCl in deionized water, as sketched in **Figure 1**a. All voltages were applied to the working electrode and are given versus Ag/AgCl. A home-built spectroelectrochemical setup was used to record steady-state absorbance spectra in the extended 500–1400 nm range for voltages ranging from +0.1 to –0.6 V versus Ag/AgCl, at temperatures ranging from 10 to 50 °C (ΔT = 10 °C). Since the potential of the Ag/AgCl electrode changes by only 0.012 V in the investigated temperature range,[17] this has a negligible effect on the applied voltage. The spectra at 30 °C are shown in Figure 1b (for more voltages see Figure S1a,

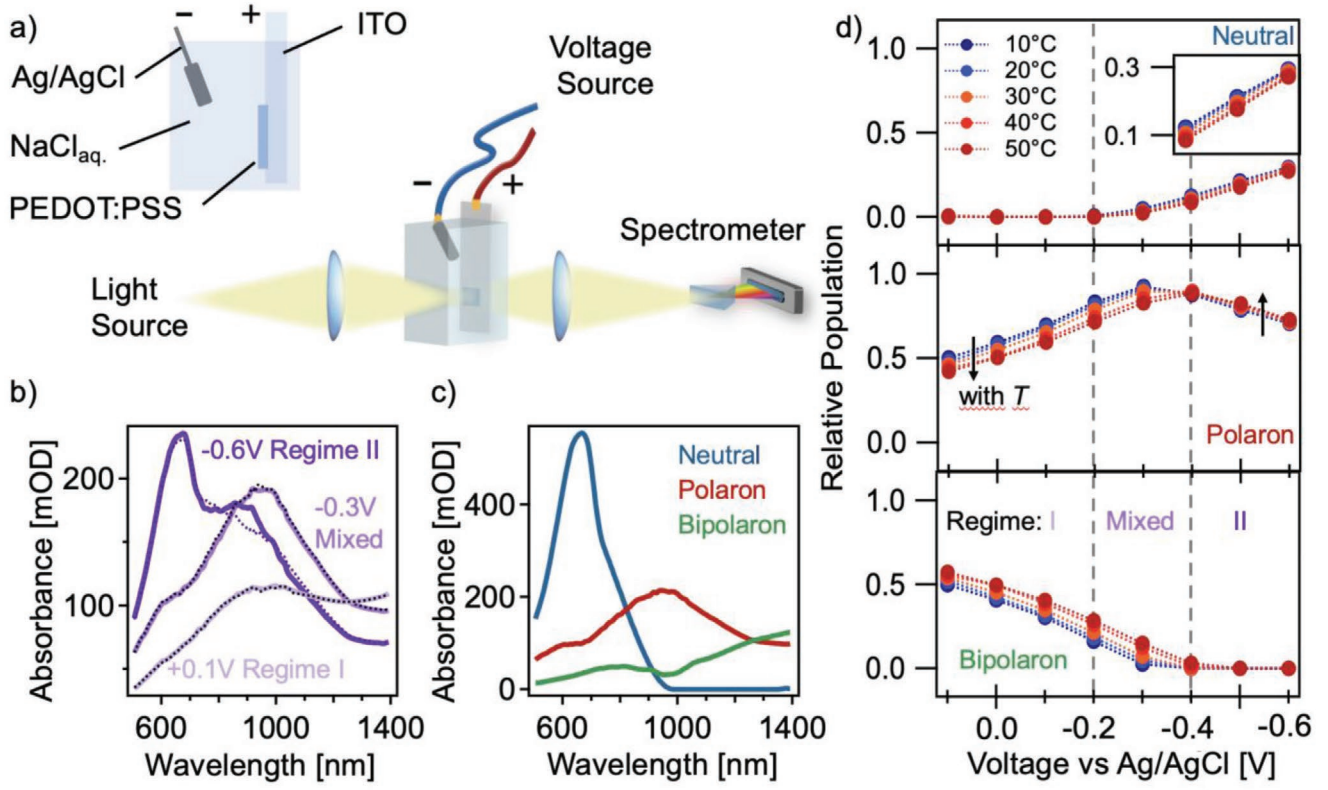

Figure 1. a) Scheme of the home-built spectroelectrochemical setup and sample configuration. b) Steady-state absorbance spectra at +0.1, –0.3, and –0.6 V versus Ag/AgCl at 30 °C, illustrating, respectively, regime I, the mixed regime, and regime II (solid lines = data, dotted lines = MCR reconstructions). c) Spectral signatures of neutral, polaron, and bipolaron states resulting from MCR deconvolution. d) Evolution of the neutral, polaron, and bipolaron populations while dedoping from +0.1 to –0.6 V versus Ag/AgCl (ΔV = 0.1 V). The black arrows indicate the evolution of the polaron population with increasing temperature.

Supporting Information). Only signatures related to PEDOT are observed, since PSS^- absorbs below 300 nm.[18]

To separate the spectral contributions of the neutral, polaron and bipolaron states, we have applied MCR analysis.[19] We have assumed a one-to-one molar conversion between the neutral, polaronic, and bipolaronic chromophores during the dedoping and redoping processes and have therefore imposed a constant total population during the MCR analysis (closure). The spectral signatures obtained for each species (Figure 1c) agree with the reported signatures and relative absorption strengths of the neutral, polaronic, and bipolaronic states of PEDOT.[8–10,14,15,20] Their linear combinations, scaled by the concentration of each species at a given voltage, fit the experimental data very well (dotted lines, Figure 1b). The absorbance peak at ≈660 nm of neutral PEDOT is dominated by transitions from the highest occupied molecular orbital to the lowest unoccupied molecular orbital.[10,14,15,20] For the polarons, the broad band centered at ≈1000 nm is attributed to the P_2 transition.[14,15] The maximum of the bipolaron absorbance at ≈1700 nm is out of the spectral range of our instrument, however, the tail of this broad band is resolved by the MCR algorithm and a second band at ≈800 nm is found. These bands are in agreements with a recent density functional theory (DFT) study and assigned to the B_1 and B_2 transitions, respectively.[14] This study also suggests the presence of oxidation states higher than +2 in PEDOT:PSS. We cannot entirely exclude this, but do not see any evidence for additional spectral components that vary with the applied voltage. Even when pushing the voltage to +0.3 V, leading to a complete depletion of the polarons, predominantly the pure bipolaron spectrum (similar to the MCR component) is seen (Figure S1b, Supporting Information).

We have determined the absorption cross-sections of the neutral, polarons, and bipolarons by relating their absorbance at different applied voltages to the injected charge density from chronoamperometry (Section S2, Supporting Information). The MCR component spectra scale with the absorption cross-sections, justifying the use of closure in the analysis and confirming that MCR concentrations are proportional to the real populations of the three species (Section S3, Supporting Information). Their relative population as a function of the applied voltage at different temperatures is displayed in Figure 1d. Due to the strong overlap between the spectral signatures, the MCR analysis offers much more reliable information about the evolution of the species compared to data sampling at a given wavelength (Figure S1c–e, Supporting Information). Three regimes can be identified. In regime I (+0.1 to −0.2 V), the PEDOT:PSS film is entirely doped, i.e., the population of neutral PEDOT is zero at all temperatures. Such a high level of doping, even in the absence of voltage (at 0 V), is considered as one of the strong advantages of PEDOT:PSS.[21] When decreasing the voltage from +0.1 to −0.2 V, the population of bipolarons decreases concomitantly with the rise of polarons, indicating the gradual reduction of bipolarons to polarons. Considering the B ⇄ P equilibrium, the equilibrium constant at 30 °C ($K_{(B\rightleftarrows P)}^{(30^\circ C)} = ln([P]/[B])$) shifts from 0.86 ± 0.07 at +0.1 V to 3.70 ± 0.30 at −0.2 V, which corresponds to a decrease of the Gibbs free energy of reaction (ΔG_r) from +0.38 ± 0.20 kJ mol^{-1} to −2.97 ± 0.20 kJ mol^{-1} according to the Van't Hoff relationship (Equation (1); values Tables S4 and S5, Section S5, Supporting Information). The uncertainty includes the errors on the MCR closure, on the MCR fit and on the Van't Hoff analysis (Sections S3—S6, Supporting Information)

$$\ln(K) = -\frac{\Delta G_r}{RT} = -\frac{\Delta H_r}{RT} + \frac{\Delta S_r}{R} \quad (1)$$

Using Equation (1) brings quantitative insights to the contributions of the enthalpy (ΔH_r) and the entropy (ΔS_r) of the reaction. We find that for all voltages in regime I, increasing the temperature from 10 to 50 °C pushes the B ⇄ P equilibrium toward the bipolarons ($[B]_{10°C} < [B]_{50°C}$ and $[P]_{10°C} > [P]_{50°C}$), indicating that the reduction of bipolarons is exothermic. At +0.1 V we deduce from the slope of the Van't Hoff plot (**Figure 2**a) that $\Delta H_{B\rightarrow P}^{+0.1V}$ has a value of −5.8 ± 0.1 kJ mol^{-1}, confirming that the enthalpy of the polarons is lower than the one of the bipolarons. Interestingly, $\Delta S_{B\rightarrow P}^{+0.1V}$ is also negative (−20.6 ± 1.7 J K^{-1} mol^{-1}), leading to an overall positive change of the free energy ($\Delta G_{B\rightarrow P}^{30^\circ C}$ = +0.38 ± 0.20 kJ mol^{-1}) where the equilibrium favours the bipolarons. As the voltage becomes more negative, the reaction becomes more exothermic ($\Delta H_{B\rightarrow P}$ more negative), while $\Delta S_{B\rightarrow P}$ also decreases to more negative values, but to a lesser extent (Figure 2b). For example, between +0.1 V and −0.2 V, $\Delta H_{B\rightarrow P}$ changes by a factor of 2.5, while $\Delta S_{B\rightarrow P}$ changes by a factor of 1.2 only. The enthalpic factor thus overcomes the entropic factor, shifting the equilibrium toward polaron formation, until the bipolarons completely vanish below −0.4 V (Figure 1d). At −0.3 V (mixed regime), the polaron reduction to neutral PEDOT also occurs and all three species coexist.

With further dedoping from −0.4 to −0.6 V (regime II in Figure 1d), the P ⇄ N equilibrium evolves toward the neutral state of PEDOT. Increasing the temperature favors the polarons ($[P]_{10\ °C} < [P]_{50\ °C}$ and $[N]_{10\ °C} > [N]_{50\ °C}$, Figure 1d), showing that polaron reduction is exothermic, similar to bipolaron reduction. Indeed, using the Van't Hoff formalism for the P⇄N equilibrium (Equation (1)), we find a negative enthalpy (responsible for the exothermicity) and a negative entropy for the forward reaction at all voltages (e.g., $\Delta H_{P\rightarrow N}^{-0.5V}$ = −4.5 ± 0.4 kJ mol^{-1} and $\Delta S_{P\rightarrow N}^{-0.5V}$ = −26.8 ± 2.0 J K^{-1} mol^{-1}, Table S7, Supporting Information). However, in contrast to the B ⇄ P equilibrium, both $\Delta H_{P\rightarrow N}$ and $\Delta S_{P\rightarrow N}$ become less negative as the voltage becomes more negative (Figure 2c). The decrease in exothermicity is compensated by the effect of $\Delta S_{P\rightarrow N}$, resulting in a decreasing but still positive $\Delta G_{P\rightarrow N}$ (+2.08 ± 0.20 kJ mol^{-1} at −0.6 V), which means that more neutral states are populated but the equilibrium remains shifted toward polarons. A further shift toward neutral species is expected at more negative voltages, which we did not apply to avoid electrolyte breakdown and sample degradation.

2.2. In Operando Time-Resolved Measurements

To understand how the neutral, polaronic, and bipolaronic states interconvert during dedoping and redoping, we measured the dynamic spectral response to a square wave voltage, switching between +0.1 and −0.6 V at different temperatures from 10 to 50 °C (ΔT = 10 °C), using the same setup (Figure 1a). The square voltage wave had a period of 2 s to ensure equilibration of the different species after the rising

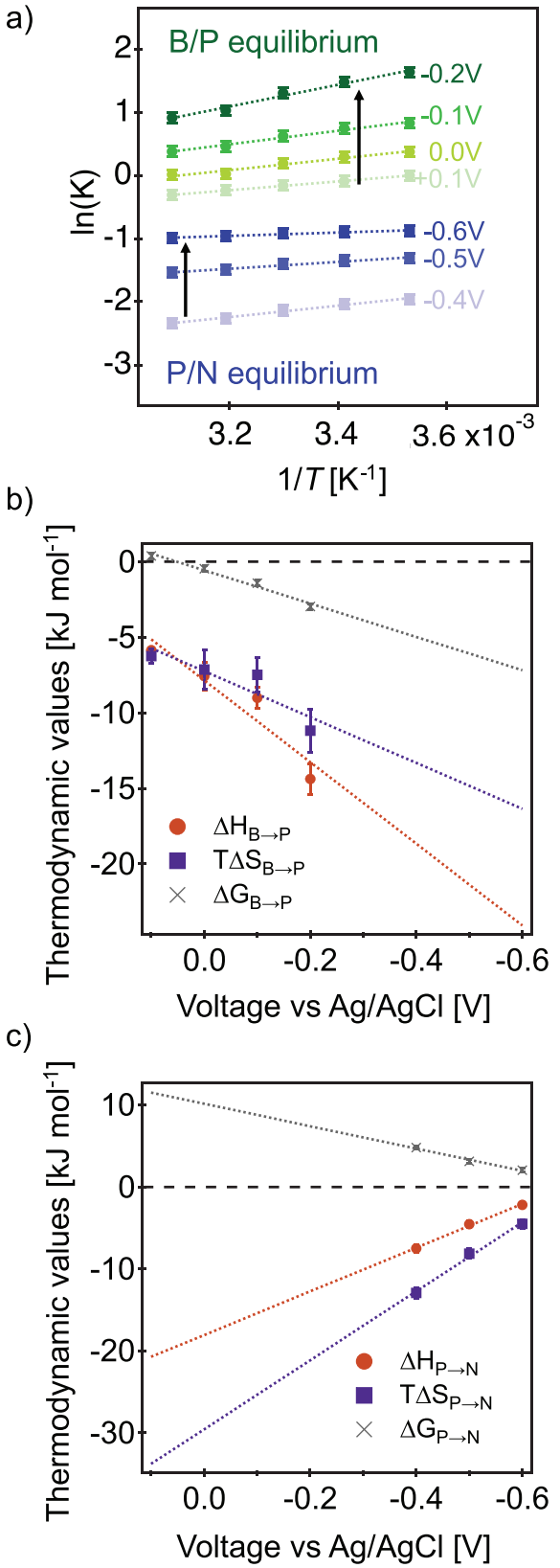

Figure 2. a) Van't Hoff plot for the B ⇄ P equilibrium from +0.1 to –0.2 V and the P ⇄ N equilibrium from –0.4 to –0.6 V. The enthalpy (ΔH_r) and entropy (ΔS_r) of the reactions are deduced from the slope and intercept, respectively. The dashed lines indicate the linear fits of the data. The error bars are included in the graphs but too small to be seen (Tables S4 and S6, Supporting Information). b,c) Evolution of the Gibbs free energy of reaction (ΔG_r) at 30 °C while dedoping (from +0.1 to –0.6 V) along with the enthalpic (ΔH_r) and entropic ($T\Delta S_r$) contribution for (b) the B ⇄ P equilibrium and (c) the P ⇄ N equilibrium. The markers indicate the experimental values, while the dashed lines are linear fits extrapolated over the full voltage range. The error bars correspond to the fitting error related to the uncertainty on the equilibrium constants K (Tables S5 and S7, Supporting Information).

or falling edge. Spectra were recorded with a time-resolution of ≈5 ms from 500 to 900 nm. From a chronoamperometric measurement of the charging current over the dedoping (+0.1 to –0.6 V) and redoping (–0.6 to +0.1 V) voltage steps, we deduced an RC time constant of the spectroelectrochemical setup of <1 ms, which does not limit the resolution of the optical measurements (Section S7, Supporting Information). To optimize the signal-to-noise ratio, we averaged the spectra over 10–20 cycles. The excellent cycle-to-cycle stability evidences the absence of degradation that might occur due to electrochemical reactions with oxygen present in the electrolyte (Section S8, Supporting Information).[22] We decomposed the time-resolved spectra using MCR analysis, yielding spectral signatures similar to the ones obtained in the steady-state measurements and more relevant dynamics of the species compared to single wavelength sampling (Sections S9 and S10, Supporting Information).

2.2.1. Dedoping Dynamics

The dedoping dynamics at 30 °C displayed in **Figure 3**a are illustrated by four representative spectral snapshots (A, B, C, D) shown in Figure 3b. Spectrum A (0 ms) corresponds to the +0.1 V steady-state spectrum, before the voltage switch, where bipolarons (55%) and polarons (45%) are in equilibrium. After the voltage switch to –0.6 V, the bipolarons rapidly reduce to polarons without any formation of neutral species until a time referred to as t_{onset} (18 ms at 30 °C). This is confirmed by the shape of spectrum B (at 11 ms) where no characteristic neutral band is visible at 660 nm. As further discussed below, t_{onset} is the delay before polarons start to be converted into neutral species. In the interval from B to C (11 to 56 ms), the bipolaron population keeps decreasing until complete depletion, while the neutral population starts to increase, as illustrated by the absorbance at 660 nm in spectrum C. At C, the neutral population has reached around 50% of its final population. As for the steady-state experiments, the neutral and bipolaron species hardly coexist. Between C and D (56 to 400 ms), an equilibrium between neutral species (30%) and polarons (70%) is established, corresponding to the steady-state situation at –0.6 V (Figure 1d).

To evaluate the rate constants of the electrochemical dedoping reactions, we built a kinetic model based on the following observations, and applied it to the concentration dynamics (Equations (1)–(6) in **Table 1**).

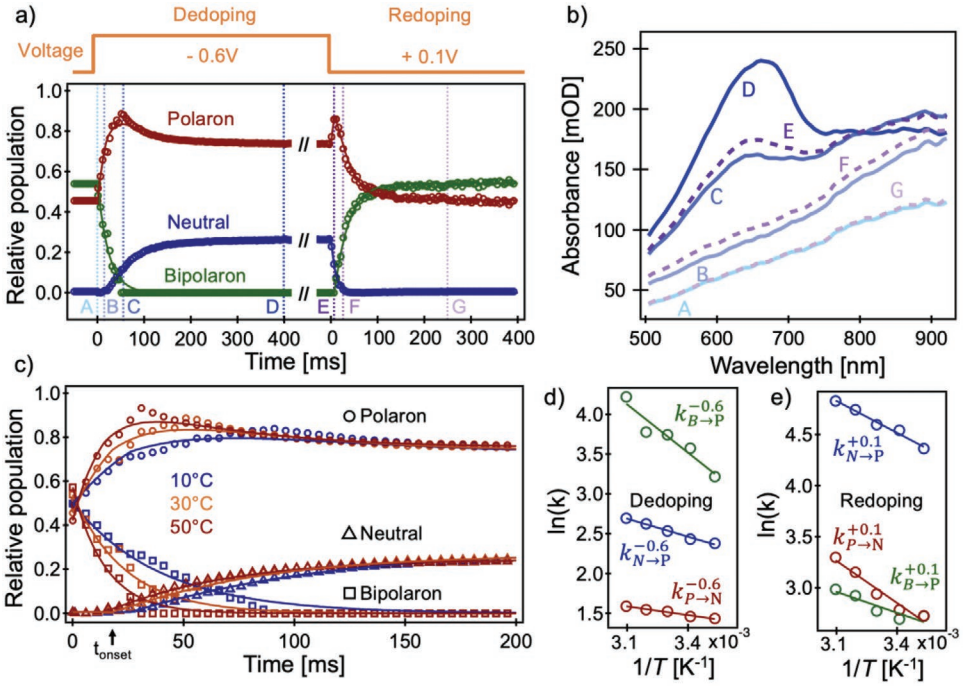

Figure 3. a) Dynamics from the MCR deconvolution of the neutral, polaron, and bipolaron populations for dedoping and redoping at 30 °C, the orange line above the graph depicts the voltage square wave applied versus Ag/AgCl. The lines are fits to the data points using the kinetic model from Table 1. The vertical dashed lines (labeled A to G) indicate specific points in the dynamics corresponding to the spectra displayed in b) A: 0 ms, B: 11 ms, C: 56 ms, and D: 400 ms for the dedoping, and E: 6 ms, F: 26 ms, and G: 250 ms for the redoping. c) Dedoping dynamics of the neutral, polaron, and bipolaron populations at 10 °C, 30 °C, and 50 °C. The lines are fits to the data points using the kinetic model from Table 1. d,e) The Arrhenius plots for the dedoping and redoping reactions, respectively.

1) The reduction of bipolarons to polarons starts without delay after the voltage switch. It follows monoexponential dynamics and is completely shifted toward product formation as one can expect from the high exergonicity of about –7.7 eV at –0.6 V (estimated from the extrapolation of $\Delta G^{-0.6}_{B\to P}$ in Figure 2b). We therefore assume a first-order reaction with respect to the bipolaron concentration for $t < t_{onset}$ (Equations (2) and (3), Table 1), meaning that the rate constant ($k^{-0.6}_{B\to P}$) describes both the bipolaron decay and the polaron rise, in agreement with previous reports.[10]
2) The conversion of polarons into neutral species starts only after t_{onset}, so that the kinetic model was split in two parts before and after this delay (Table 1).
3) After t_{onset}, the establishment of the P ⇄ N equilibrium requires to introduce the forward and backward rate constants $k^{-0.6}_{P\to N}$ and $k^{-0.6}_{N\to P}$, respectively. Since their ratio is equal to the equilibrium constant $K^{-0.6}_{P\rightleftarrows N}$, we substituted $k^{(-0.6)}_{(N\to P)} = k^{(-0.6)}_{(P\to N)} / K^{(-0.6)}_{(P\rightleftarrows N)}$ in the first-order rate equations (Equations (4) and (5), Table 1). $K^{-0.6}_{P\rightleftarrows N}$ is the [P]/[N] ratio in the steady state (at point D).

The implementation of the kinetic model, using an open-source Python package,[23] and the determination of t_{onset} are described in detail in Section S11 of the Supporting Information. The resulting rate constants are summarized in **Table 2**. Slight discrepancies in $K^{-0.6}_{P\rightleftarrows N}$ obtained from the time-resolved measurements (Table 2) compared to the steady-state

Table 1. Differential rate equations describing the dedoping dynamics. The relative neutral, polaron, and bipolaron concentrations are represented by [N], [P], and [B], respectively. For the rate constants (k), the superscript (–0.6) indicates the applied voltage versus Ag/AgCl in volt, while the subscript shows the relevant reaction step.

For $t < t_{onset}$		For $t > t_{onset}$	
$\frac{d[N]}{dt} = 0$	(1)	$\frac{d[N]}{dt} = k^{-0.6}_{P\to N}[P] - (k^{-0.6}_{P\to N} / K^{-0.6}_{P\rightleftarrows N})[N]$	(4)
$\frac{d[P]}{dt} = k^{-0.6}_{B\to P}[B]$	(2)	$\frac{d[P]}{dt} = k^{-0.6}_{B\to P}[B] - k^{-0.6}_{P\to N}[P] + (k^{-0.6}_{P\to N} / K^{-0.6}_{P\rightleftarrows N})[N]$	(5)
$\frac{d[B]}{dt} = -k^{-0.6}_{B\to P}[B]$	(3)	$\frac{d[B]}{dt} = -k^{-0.6}_{B\to P}[B]$	(6)

Table 2. Rate and equilibrium constants of the electrochemical reactions involved in dedoping (–0.6 V) and redoping (+0.1 V) at 10 °C, 20 °C, 30 °C, 40 °C, and 50 °C obtained via kinetic modeling on the concentration dynamics found with MCR. The onset time of neutral formation during dedoping (t_{onset}) and of bipolaron formation during redoping (t'_{onset}) is also given.

		10 °C	20 °C	30 °C	40 °C	50 °C
Dedoping	$k^{-0.6}_{B\to P}$ [s^{-1}]	25.0	35.7	42.3	43.7	68.1
	$k^{-0.6}_{P\to N}$ [s^{-1}]	4.2	4.3	4.6	4.7	4.9
	$k^{-0.6}_{N\to P}$ [s^{-1}]	10.8	11.4	12.6	13.8	14.8
	$K^{-0.6}_{P\rightleftarrows N}$	0.39	0.38	0.36	0.35	0.33
	t_{onset} [ms]	26	18	18	18	14
Redoping	$k^{+0.1}_{N\to P}$ [s^{-1}]	78.7	94.0	99.3	115.0	125.4
	$k^{+0.1}_{P\to B}$ [s^{-1}]	15.3	16.2	18.9	23.4	27.1
	$k^{+0.1}_{B\to P}$ [s^{-1}]	15.2	14.8	16.0	18.6	19.8
	$K^{+0.1}_{P\rightleftarrows B}$	1.00	1.10	1.18	1.26	1.37
	t'_{onset} [ms]	5	6	7	9	11

measurements (Table S6, Supporting Information) originate from sample-to-sample variations and from the different spectral ranges used that influence the MCR analysis. As shown in Figure 3c and Figures S23 and S27 (Supporting Information), the model allows a good reproduction of the dynamics at different temperatures. Considering the data at 30 °C, the initial reduction of bipolarons to polarons ($\tau^{-0.6}_{B\to P} = 1/k^{-0.6}_{B\to P}$ = 24 ms) is much faster than the second step establishing the final equilibrium between polarons and neutral species ($\tau^{-0.6}_{P\to N}$ = 217 ms). The back reaction ($\tau^{-0.6}_{N\to P}$ = 79 ms) is also faster than the forward reaction, in agreement with the equilibrium being shifted toward the polarons (Figure 2c, $\Delta G_{P\to N} > 0$ at –0.6 V).

An acceleration of the kinetics with temperature is observed in the MCR dynamics (Figure 3c) and reflects in the rate constants in Table 2. This increase is more pronounced for the conversion of bipolarons into polarons, where an Arrhenius plot (Figure 3d) allows to determine an activation energy (E_a) of 16.8 kJ mol^{-1} (**Table 3**). E_a is smaller for the P → N and N → P reactions, with values of 3.0 and 6.2 kJ mol^{-1}, respectively (the lower forward barrier is in agreement with the reaction being exothermic). The faster rate of the bipolaron reduction in spite of the higher activation energy can be explained by the larger pre-exponential factor (A), which is linked to the entropy of activation. We use transition state theory (Eyring model) to convert E_a to the enthalpy of activation ($\Delta H^{\ddagger}$) and A to the entropy of activation ($\Delta S^{\ddagger}$) according to Equations (2) and (3), assuming first-order one-step reactions[24–26]

$$\Delta H^{\ddagger} = E_a - RT \tag{2}$$

$$\Delta S^{\ddagger} = R \times \ln\left(\frac{Ah}{2.718 \times k_B T}\right) \tag{3}$$

Here, k_B, h, and R are respectively the Boltzmann, Planck, and universal gas constants. The values obtained at 30 °C are given in Table 3 and are discussed in detail in Section 3. We find that the Gibbs free energy of activation ($\Delta G^{\ddagger} = \Delta H^{\ddagger} - T\Delta S^{\ddagger}$) explains the observed trends in the reaction kinetics. Thus, $\Delta G^{\ddagger}$ inversely scales with the rate constants obtained for the different processes ($\Delta G^{\ddagger 0.6}_{B\to P} < \Delta G^{\ddagger 0.6}_{N\to P} < \Delta G^{\ddagger 0.6}_{P\to N}$ and $k^{-0.6}_{B\to P} > k^{-0.6}_{N\to P} > k^{-0.6}_{P\to N}$). The reported worst-case errors in Table 3 include the uncertainties on the equilibrium constants, on the kinetic model fits and on the Arrhenius analysis (Section S12, Supporting Information). The error on the activation parameters is typically <15%.

2.2.2. Redoping Dynamics

For redoping, the voltage is switched from –0.6 to +0.1 V. The steady-state P ⇄ N equilibrium before the switch is represented

Table 3. Arrhenius parameters (ln(A) and E_a) extracted from the temperature-dependence of the rate constants with the related enthalpy, entropy, and Gibbs free energy of activation calculated with Equations (2) and (3) at 30 °C ≃ 303 K (Section S12, Tables S14 and S16, Supporting Information).

	Dedoping (+0.1 to –0.6 V)			Redoping (–0.6 to +0.1 V)		
	B → P	P → N	N → P	N → P	P → B	B → P
ln(A) [s^{-1}]	10.4 ± 1.3	2.7 ± 0.2	5.0 ± 0.4	8.0 ± 0.3	7.5 ± 0.7	5.1 ± 0.5
E_a [kJ mol^{-1}]	16.8 ± 3.2	3.0 ± 0.8	6.2 ± 0.7	8.5 ± 0.7	11.4 ± 2.2	5.7 ± 2.4
$\Delta H^{\ddagger}$ [kJ mol^{-1}]	14.2 ± 3.2	0.5 ± 0.8	3.7 ± 0.7	6.0 ± 0.7	8.9 ± 2.2	3.2 ± 2.4
$\Delta S^{\ddagger}$ [JK^{-1} mol^{-1}]	–167.1 ± 11.3	–230.8 ± 2.0	–211.7 ± 3.2	–186.8 ± 2.5	–190.8 ± 6.3	–211.1 ± 6.4
$\Delta G^{\ddagger}$ [kJ mol^{-1}]	64.9 ± 5.8	70.4 ± 0.9	67.9 ± 1.5	62.6 ± 1.5	66.7 ± 3.0	67.1 ± 3.2

by spectrum D in Figure 3b. At 30 °C, 6 ms after the switch (spectrum E), about half of the neutral population is oxidized to the polaronic state. The bipolarons are formed only after a delay (t'_{onset}) of 7 ms. After 26 ms (spectrum F), the neutral population is completely depleted, and the absorbance spectrum is exclusively composed of polaron and bipolaron signatures. The oxidation of polarons to bipolarons continues until a complete recovery of the initial B ⇄ P equilibrium at +0.1 V (spectrum G = A). We have implemented a comparable kinetic model as for the dedoping dynamics, with $N \rightarrow P \rightleftarrows B$, assuming first-order reaction kinetics and a delayed bipolaron formation (see Section S11, Supporting Information). At 30 °C, the oxidation of neutral PEDOT occurs with a time constant of $\tau^{+0.1}_{N\rightarrow P} = 10$ ms, which is twice as fast as the fastest dedoping step ($\tau^{-0.6}_{B\rightarrow P} = 24$ ms). From the temperature-dependence (Figure 3e), we deduce an activation energy and Gibbs free energy of activation of $E_a = 8.5 \pm 0.7$ kJ mol^{-1} and $\Delta G^{\ddagger} = 62.6 \pm 1.5$ kJ mol^{-1} (Table 3), respectively. Thus, it is again the relatively low $\Delta G^{\ddagger}$ that causes the fast rate of the N → P reaction. The time constants of the B ⇄ P equilibrium are $\tau^{+0.1}_{P\rightarrow B} = 53$ ms and $\tau^{+0.1}_{B\rightarrow P} = 63$ ms (at 30 °C), being slower than the initial N → P conversion at +0.1 V, but faster than the establishment of the N ⇄ P equilibrium during dedoping at –0.6 V, which can be correlated to differences in the free energy of activation (Table 3). The faster redoping dynamics compared to the dedoping dynamics and the general trends between reactions are consistent with a previous report,[10] but our rate constants are 50–200 times faster. This disparity is likely due to the differences in dimensions and morphology of the sample.[10]

3. Discussion

The redox reactions in PEDOT:PSS that we monitor here via spectroscopy are accompanied by an intricate interplay of ionic and electronic transport. Upon dedoping, Na^+ cations penetrate the PEDOT:PSS film and compensate the charges on PSS^-, allowing the bipolarons ($PEDOT^{2+}$) and polarons ($PEDOT^+$) to be reduced by electrons injected from the ITO working electrode. Upon redoping, Na^+ cations are expulsed, so that the more oxidized species (polarons, bipolarons) are again stabilized by uncompensated PSS^-. Morphologically, PEDOT-rich domains favor the electronic transport and are embedded in a permeable PSS-rich matrix, where the hydrated ions can easily move.[8,12,27] The oxidized segments of PEDOT are localized on 6–7 monomers and show a quinoidal backbone more planar than for aromatic neutral $PEDOT^0$.[14] Moreover, larger structural changes accompany the redox reactions, due to the local changes in backbone conformation and ion intercalation between the polymer chains. Recently, time-resolved in situ GIWAXS measurements have revealed that doped PEDOT shows more ordered and contracted π-stacking together with an expansion of the lamellar packing compared to the undoped state.[10] The reversible change of the out-of-plane lamellar spacing (d_{100}) was found to follow the conversion between polaronic and bipolaronic species.

Here, we observe that the initial dedoping (B → P) and redoping (N → P) steps start immediately after the corresponding voltage switch and follow monoexponential dynamics until complete depletion of the reactant. This implies that the processes have a first-order dependence on the bipolaron and neutral concentrations, respectively, and are not limited by the transport of Na^+ in the film (this would follow more complex diffusion-limited dynamics).[24,25] Hence, we assume that for films with a thickness of only 100 nm (as studied here) and voltages of –0.6/+0.1 V (de/redoping), the ion penetration/expulsion is much faster than the electrochemical redox reactions of PEDOT, which occur at the ITO electrode. This agrees with the high reported mobility of Na^+ in PEDOT:PSS (9.3×10^{-4} cm^2 V^{-1} s^{-1}, as high as in water).[8,28] We were able to omit the concentration of Na^+ cations in our kinetic model, which indicates that they do not directly participate in the rate-limiting electrochemical step, but rather create an overall dielectric environment that favors the redox reactions.[24,25] In line with this, the ionic and electronic charges do not necessarily evolve in the same morphological regions, as it has been suggested that the ions mostly accumulate at the boundaries between PSS-rich and PEDOT-rich domains of PEDOT.[11–13] Similarly in P3HT, ions first integrate more amorphous polymer regions while polarons are formed in segregated more crystalline domains.[29]

Within the investigated voltage range, we completely deplete the bipolaron population (at –0.6 V) and neutral population (at +0.1 V), but we never reach a regime where all polarons disappear. Instead, relatively slow establishments of a $P \rightleftarrows N$ equilibrium (dedoping) and a $P \rightleftarrows B$ equilibrium (redoping) are observed. Both equilibria are predominantly determined by the thermodynamics of the system, since the energy levels smoothly shift with the temperature (Van't Hoff plot, Figure 2a) and the applied voltage (Nernst-type behavior, Figure 2b,c). An extrapolation suggests that complete reduction/oxidation of polarons can be reached at higher absolute voltage and indeed only bipolarons are observed when the voltage is pushed to +0.3 V (Figure S1b, Supporting Information). Therefore, it is unlikely that there is a limit where some polarons remain unavailable to participate in the redox reactions (because they are in morphological regions inaccessible to ionic and/or electronic transport).[30] We conclude that the doping level at a given voltage is determined by thermodynamics rather than limited by morphological inhomogeneities. Moreover, the remaining polarons at negative voltages could be due to permanent oxygen doping of the film,[22] but this would imply a saturation of the $P \rightleftarrows N$ equilibrium constant and a nonlinear dependence of $\Delta G_{P\rightarrow N}$ on the voltage (not seen in Figure 2c). Thus, any oxygen doping is discharged during the initial precycling of the device and does not have time to build up again at the 2 s cycling speed. The establishment of the $P \rightleftarrows N$ and $P \rightleftarrows B$ equilibria can again be modeled by first-order kinetic processes, showing that ion-diffusion plays a minor role in limiting the reactions. Only a very slight deviation from monoexponential dynamics is found (e.g., in the rise of the neutral population during dedoping, Figure S32, Supporting Information), possibly indicating a slower conversion within more crystalline PEDOT regions where ion diffusion is slower.[8]

Interestingly, for both the dedoping and redoping dynamics, the electrochemical conversion of the polarons ($P \rightleftarrows N$ *or* $P \rightleftarrows B$) starts only after a certain latency time (dedoping: t_{onset}, redoping: t'_{onset}). For example during dedoping, we know that around 50% of polarons are already present in the doped state

at the moment of the voltage switch, but these polarons cannot be oxidized to neutral states before t_{onset}. It is unlikely that these delays are related to a slow polarization of the electrolyte (i.e., accumulation of opposite ions at the counter electrode and inside the film), given the < 1 ms RC time of the system and since the initial reactions (B → P and N → P) are triggered immediately, evidencing fast ionic transport. For the dedoping, t_{onset} decreases with increasing temperature (Table 2) and always occurs when the polaron concentration reaches ≈75% (Figure S22, Supporting Information). For the redoping, t'_{onset} increases with temperature (Table 2) and occurs at a polaron concentration of 80–95% (Figure S26, Supporting Information). More investigations will be necessary to elucidate the precise origin of this delay. One hypothesis that we propose here is that a certain concentration of polarons (reached at $t^{(')}_{onset}$) is necessary to induce large-range structural changes in the packing of the PEDOT chains, such as have been observed during the B → P conversion by time-resolved Grazing-Incidence Wide-Angle X-ray Scattering (GIWAXS) measurements,[10] and that those morphological changes are needed before the next redox step can proceed toward the final equilibrium.

The electrochemical reactions that we probe here occur at the ITO electrode and consist of the charge transfer between the electrode and PEDOT. The injection itself should not be limiting, since the contacts are ohmic.[31] By the time we measure the optical signatures of the redox species with 5 ms resolution, they are distributed throughout the bulk of the film, but this is not a limiting process since transport over a 100 nm film occurs on the sub-ms time scale given the high mobility of holes in PEDOT:PSS. The thermodynamics of the reactions will depend on the potential of the electrode and the energy level of the involved PEDOT redox state, which varies with applied voltage and is not the same for neutral, polarons, and bipolarons, due to enthalpic and entropic effects. For example, the different redox species will have different stabilization by the ions, different intermolecular packing and different delocalization. The rate of the charge transfer also depends on these energy levels as well as on structural re-organization of the PEDOT, according to the Marcus formalism.

Figure 4 summarizes the reaction and transition state thermodynamics for the dedoping (solid lines) and redoping (dashed lines) processes, as obtained by the Van't Hoff and Eyring analysis. For comparison purposes, since the absolute energies are not known, the levels are plotted relatively to the neutral level, which is always set to zero. The reaction profiles of the Gibbs free energy explain the full thermodynamic and kinetic behavior of the system: the relative levels of the three redox species drive the reactions and determine the doping level at a given voltage, while the activation barriers set the rate of the electrochemical processes. More insights can then be gained by considering the entropic and enthalpic contributions.

When dedoping at −0.6 V (B → P ⇄ N), the entropic contribution to the free energy of reaction is unfavorable ($-T\Delta S$ increases for both reduction steps), but this is compensated by the favourable enthalpic contribution, with both the B → P and P → N conversions being exothermic. Concerning the higher entropy of the bipolarons and polarons with respect to the neutral state, we suggest that the quinoid backbone planarization and better π-stacking of the charged segments enhances the electronic delocalization,[10,14,32] increasing the density of states and therefore the entropy, despite the higher morphological order. Moreover, the bipolarons entropically benefit from a larger number of states with a different carrier arrangement compared to the polarons.[33] For the enthalpy, since no covalent bonds are broken or formed, it is dominated by electrostatic interactions with the environment (mobile ions, PSS^-, other (bi)polarons) and intermolecular changes in PEDOT chain packing. In agreement with the observed drop in enthalpy during depoping, the more reduced forms (polarons, neutral) are electrostatically stabilized at −0.6 V, where Na^+ ions inside the film compensate the PSS^-. The large drop in enthalpy between bipolarons and polarons could also be related to the reported change in lamellar spacing during this process.[10] While dedoping is driven by enthalpy, the opposite is true for redoping (N → P ⇄ B) at +0.1 V, where the conversion toward bipolarons is strongly favored by the increase in entropy, which is even enhanced at +0.1 V compared to −0.6 V. The redoping is enthalpically unfavorable, although we expect the oxidized PEDOT species to be stabilized by the PSS^- ions when the Na^+ ions are expulsed from the film at +0.1 V. We suggest that the enthalpy is determined by an interplay between stabilizing electrostatic attractions to the PSS^- anions and destabilizing repulsions with other positively charges polarons and/or bipolarons as their density increases at +0.1 V.

Now focusing on the reaction dynamics, we have seen that the dedoping reactions are slower than the redoping reactions, with the first irreducible redox step always being faster than the establishment of the final equilibrium. Overall, it is always the conversion of the polarons either to neutral or bipolaronic states that limits the rate of the dedoping and redoping reactions, respectively. The trends in the reaction kinetics can be explained by the height of the free energy activation barrier, which depends on the applied voltage. The entropic contribution ($\Delta S^{\ddagger}$) plays a predominant role and accounts for 78–99% of $\Delta G^{\ddagger}$ (Figure S33, Supporting Information), so that considering only $\Delta H^{\ddagger}$ (or E_a) is not sufficient. Apart from the B → P conversion (where drastic structural changes occur),[10] $\Delta H^{\ddagger}$ is generally very small (Figure 4), in agreement with electrochemical reactions that do not involve any covalent bond formation or breaking. $\Delta S^{\ddagger}$ is negative for all dedoping and redoping reaction steps, indicating transition states with lower entropy (i.e., more rigid, less delocalized) compared to the reactants.[25] The important entropic barriers are likely related to changes in backbone conformation (aromatic/quinoid) that impact the bond-length alternation (charge delocalization) and the packing of the PEDOT chains during the electrochemical reactions. In particular, we note the large entropy of activation for the P → N conversion during the dedoping process at −0.6 V (Table 3), which causes the slowest of all observed rates (Table 2). Since it has been shown by chronoamperometry that the charge injected into an OECT channel follows the build-up of the neutral state during dedoping,[10] we conclude that entropically slow electrochemical steps can have a decisive impact on OECT switching speed when ion diffusion is not the limiting parameter.

4. Conclusion

In this work, we have examined the electrochemical dedoping and redoping reactions of a thin PEDOT:PSS film immersed

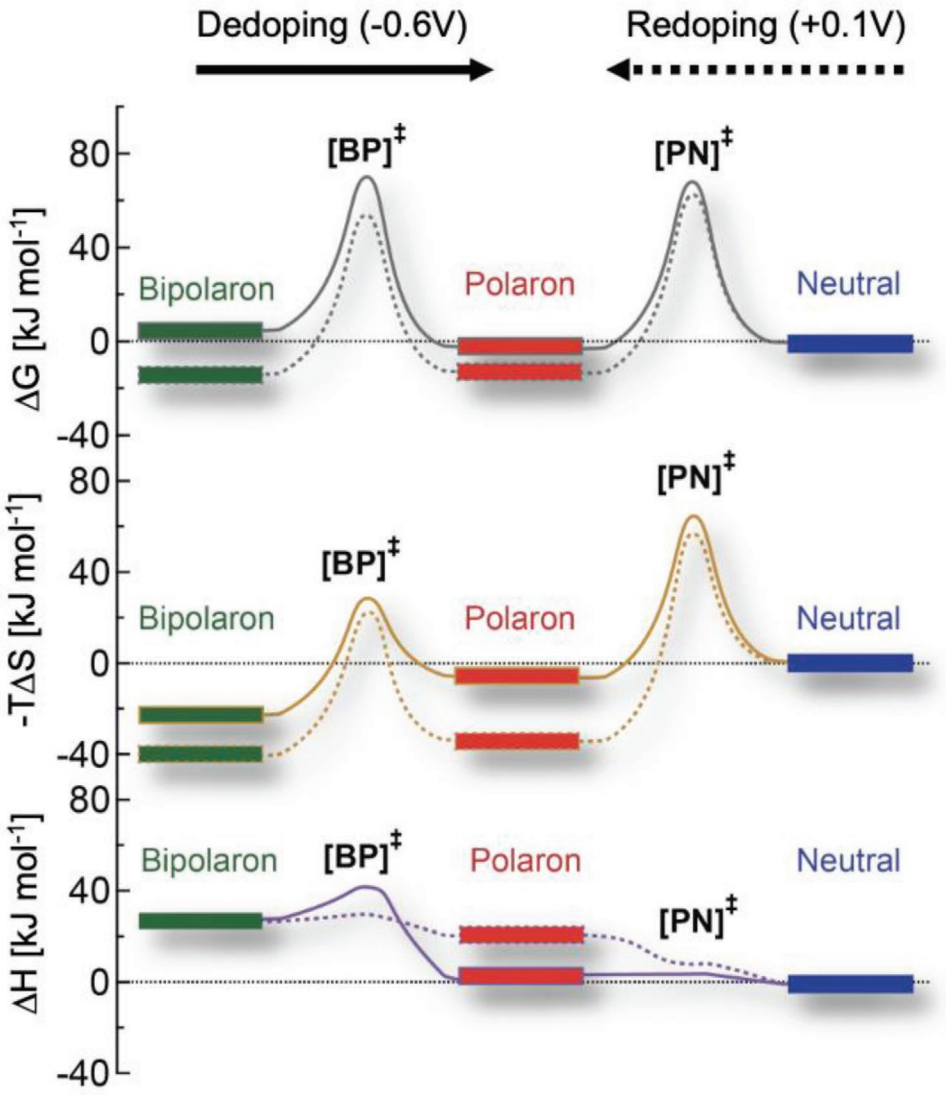

Figure 4. Energetic reaction profiles for the dedoping reaction (solid lines) and the redoping reactions (dashed lines), showing the entropic and enthalpic contributions to the overall Gibbs free energy. The Gibbs free energy (ΔG_r), entropy (ΔS_r), and enthalpy (ΔH_r) of the reactions were obtained from the Van't Hoff analysis (Tables S5 and S7, relatively to the neutral level), while the Gibbs free energy ($\Delta G^{\ddagger}$), entropy ($\Delta S^{\ddagger}$), and enthalpy ($\Delta H^{\ddagger}$) of activations originate from the Eyring model applied on the Arrhenius parameters (Table 3). The energy levels for the bipolaronic and neutral states were determined at –0.6 and +0.1 V, respectively, using the extrapolations displayed in Figure 2.

in NaCl electrolyte, using steady-state and time-resolved spectroelectrochemistry. Careful deconvolution of the spectra using MCR analysis has allowed to separate the overlapping absorption signatures of the neutral (N), polaron (P), and bipolaron (B) states of PEDOT, so that their relative populations could be evaluated as a function of applied voltage and temperature. We found that the doping level (i.e., concentration of the different redox species at a given voltage) depends on thermodynamical equilibria that are ruled by the Gibbs free energy of the reactions. Moreover, we followed the dynamics of the dedoping after a fast voltage switch to –0.6 V and of the redoping when switching the voltage back to +0.1 V. The dedoping is driven by enthalpy (electrostatic destabilization of the electronic charges when Na^+ ions penetrate the film and compensate the PSS^- anions), while the redoping is driven by entropy (higher delocalization and a higher density of states in the charged species). Our kinetic modeling of the data revealed sequential first-order electrochemical reactions (dedoping: $B \rightarrow P \rightleftarrows N$, redoping: $N \rightarrow P \rightleftarrows B$). Thus, in our experimental conditions, the ion diffusion is much faster than the redox reactions and does not limit the dynamics. Finally, an analysis of the temperature-dependence of the kinetics allowed to extract the activation parameters, showing that the activation entropy is the predominant parameter influencing the reaction rates. Generally, redoping is faster than dedoping and both processes are rate limited by the establishment of the final equilibrium. Our approach is relevant to understand the intrinsic device switching speed that can be achieved in situations where ion diffusion is not the slowest process. We expect that further structural characterization and theory will bring further insights

to the microscopic parameters that can control the entropy and therefore the speed of in OMIEC-based devices. Molecular engineering with a special focus on the entropy then promises further enhancement of the response time of electrochemical systems like OECTs, biosensors or neuromorphic devices.

5. Experimental Section

Sample Preparation: Dodecylbenzene sulfonic acid (0.002 vol%), (3-glycidyloxypropyl)trimethoxysilane (1 wt%), and ethylene glycol (5 vol%) were added to a PEDOT:PSS aqueous suspension (Clevios PH-1000 from Heraeus Holding GmbH) as reported.[2,8] Before deposition, the solution was sonicated for 40 min at room temperature and filtered using 0.8 µm syringe filters (Minisart from Sarrorius AG). The ITO-covered glass substrates (S111 from Ossila) were cleaned with a water-based cleaning solution (2% Hellmanex III from Hellma), acetone and isopropanol before activation with UV/O_3. The depositions were performed by spin-coating at 2500 rpm for 90 s. After deposition, the films were annealed at 140 °C for 45 min. The thickness of PEDOT:PSS films was determined to be 107 ± 4 nm via three measurements at different film positions using a white light interferometer (ContourGT-K from Brucker). The PEDOT:PSS films were then delimited to an area of 4 × 4 mm using a razor blade. For the chronoamperometry, a new PEDOT:PSS film was spin-coated on the ITO-covered glass substrate. A similar PEDOT:PSS solution as for the temperature-dependent measurements was used. The film area (≈4.3 mm^2) was delimitated using high-precision swabs (C201 from Ossila). The film thickness was 240 ± 2 nm and the total film volume was about 10.32×10^{-7} cm^3.

Spectroelectrochemical Setup: The home-made setup was composed of a halogen light source (HL-2000 from Ocean Insight), a vis–NIR spectrophotometer (Flame Vis-NIR from Ocean Insight), and an NIR spectrophotometer (Flame NIR from Ocean Insight). The light beam was directed through optical fibers, lenses, and a dichroic mirror (from Thorlabs). The spectrophotometer acquisition was externally triggered by a Digital Delay Generator (DG535 from Stanford Research Systems). The voltage was applied via a DAQ device (USB-6008 from National Instrument Corp.). Communication with the instruments and user interface were implemented with a custom LabView software. The ITO slide coated with PEDOT:PSS (working electrode) was immersed together with a Ag/AgCl pellet reference/counter electrode (Warner Instruments) in a 1 cm cuvette containing 0.1 M NaCl in deionized water. The cuvette temperature was regulated using a TC-125 from Quantum Northwest temperature controller.

Steady-State and Time-Resolved Measurements: Steady-state measurements were performed by applying a constant voltage. After stabilization, a steady-state spectrum was recorded using both spectrophotometers. Time-resolved measurements were performed using only the vis–NIR spectrophotometer to gain in time resolution. Measurements were performed using 20 pulses of square wave voltage from +0.1 to −0.6 V with a period of 2 s (pulse width = 1 s). Few cycles were removed due to bad time overlap between the voltage pulses (Figure S13, Supporting Information). The spectra of the appropriate cycles were averaged, offering a time-resolution of ≈5 ms.

Chronoamperometry Coupled to Vis–NIR Absorbance Spectroscopy: Square-pulses of voltages, stepping up from −0.3 to +0.6 V (ΔV = +0.1 V vs Ag/AgCl) were applied at the Ag/AgCl gate (quasi-reference electrode) by a data acquisition system (USB-6211 from National Instrument Corp.). The time-dependent current resulting from each voltage step was converted into a voltage using a low-noise current preamplifier (SR570 from Stanford Research Systems) and measured with the USB-6211 acquisition system with a time-resolution of 16 µs. Each voltage step was held for 3 s (= pulse width) to ensure steady states. Subsequently, steady-state absorbance spectra were acquired in order to correlate the measured current to the species present in the film. For this experiment, the spectrophotometer acquisition was externally triggered using the USB-6211 system. Communication with the instruments and the user interface were implemented with a custom LabView software.

MCR: MCR analysis allowed the decomposition of overlapping spectral signatures and the elucidation of the relative abundance of the different species from a data set containing a mixture of species.[19,34] MCR techniques are typically expressed as a matrixial equation

$$D = C \cdot S^{T} + E \tag{4}$$

where D is a data set containing the evolution of the concentrations C of pure spectra S^T and E is the error not expressed by the product $C \cdot S^T$. From initial guesses, both C and S^T are alternatively optimized to reach the best fit with D (i.e., minimization of E). In this case, the open-source python library pyMCR was used.[19] For the steady-state voltage measurements, MCR was performed on the spectra measured at different voltages. Thus, the D matrix consists of all the steady-state spectra at different voltages concatenated together. As spectral initial guesses (S^T) of the neutral, polaron, and bipolaron species, three gaussians were used respectively centered at 650 nm, 1000 nm and 1400 nm. Concerning the concentrations (C), any initial guesses were not used, but the "closure": [N] + [P] + [B] = 1 was applied. This constraint corresponds to the mathematical implementation of the mass balance criterium (i.e., that upon oxidation the total number of PEDOT fragment is fixed but the distribution of the three species changes).[19,35] Its use is justified in detail in Sections S2—S4 of the Supporting Information. For the time-resolved measurements, the MCR deconvolution with fixed spectral initial guesses obtained from the deconvolution of the steady-state measurements was performed, keeping the same ratio between the signatures (Figure S15, Supporting Information).

Supporting Information

Supporting Information is available from the Wiley Online Library or from the author.

Acknowledgements

The authors thank the European Research Council (ERC) for supporting this research by a Starting Grant (No. 714586, OSIRIS) and acknowledge NCCR-MUST, a research instrument of the Swiss National Science Foundation, as well as the University of Bern.

Open access funding provided by Universitat Bern.

Conflict of Interest

The authors declare no conflict of interest.

Author Contributions

G.R. fabricated the samples and performed all experiments. J.A. contributed to the preliminary experiments leading to this work. G.R., O.B., and J.R. built the spectroelectrochemical setup and its LabVIEW interface. G.R. performed the MCR, Eyring, Van't Hoff, and Arrhenius analysis and developed the kinetic model. All authors contributed to data interpretation. G.R. and N.B. wrote the manuscript with contributions from O.B. and J.R. All authors have given approval to the final version of the manuscript.

Data Availability Statement

The data that support the findings of this study are openly available in BORIS at https://boris.unibe.ch/id/eprint/156948.

Keywords

doping mechanisms, multivariate curve resolution, organic electrochemical transistors, organic-mixed ionic–electronic conductors, temperature-dependence, time-resolved spectroelectrochemistry

Received: June 16, 2021
Revised: September 1, 2021
Published online:

[1] B. D. Paulsen, K. Tybrandt, E. Stavrinidou, J. Rivnay, *Nat. Mater.* **2020**, *19*, 13.
[2] S. Inal, G. G. Malliaras, J. Rivnay, *Nat. Commun.* **2017**, *8*, 1767.
[3] J. Rivnay, R. I. M. Owens, G. G. Malliaras, *Chem. Mater.* **2014**, *26*, 679.
[4] a) R. Smith, *Ph.D. Thesis*, University of Surrey, **2019**; b) Y. Wang, C. Zhu, R. Pfattner, H. Yan, L. Jin, S. Chen, F. Molina-Lopez, F. Lissel, J. Liu, N. I. Rabiah, *Sci. Adv.* **2017**, *3*, e1602076; c) Y. Ma, Y. Zhang, S. Cai, Z. Han, X. Liu, F. Wang, Y. Cao, Z. Wang, H. Li, Y. Chen, *Adv. Mater.* **2020**, *32*, 1902062; d) Y. Wen, J. Xu, *J. Polym. Sci., Part A: Polym. Chem.* **2017**, *55*, 1121.
[5] D. Khodagholy, J. N. Gelinas, T. Thesen, W. Doyle, O. Devinsky, G. G. Malliaras, G. Buzsáki, *Nat. Neurosci.* **2015**, *18*, 310.
[6] B. Ji, M. Wang, C. Ge, Z. Xie, Z. Guo, W. Hong, X. Gu, L. Wang, Z. Yi, C. Jiang, *Biosens. Bioelectron.* **2019**, *135*, 181.
[7] N. Fani, M. Hajinasrollah, M. Asghari Vostikolaee, M. Baghaban Eslaminejad, F. Mashhadiabbas, N. Tongas, M. Rasoulianboroujeni, A. Yadegari, K. Ede, M. Tahriri, *J. Bioact. Compat. Polym.* **2019**, *34*, 436.
[8] J. Rivnay, S. Inal, B. A. Collins, M. Sessolo, E. Stavrinidou, X. Strakosas, C. Tassone, D. M. Delongchamp, G. G. Malliaras, *Nat. Commun.* **2016**, *7*, 11287.
[9] X. Wu, A. Surendran, J. Ko, O. Filonik, E. M. Herzig, P. Müller-Buschbaum, W. L. Leong, *Adv. Mater.* **2019**, *31*, 1805544.
[10] B. D. Paulsen, R. Wu, C. Takacs, H.-G. Steinrück, J. Strzalka, Q. Zhang, M. Toney, J. Rivnay, *Adv. Mater.* **2020**, *32*, 2003404.
[11] A. V. Volkov, K. Wijeratne, E. Mitraka, U. Ail, D. Zhao, K. Tybrandt, J. W. Andreasen, M. Berggren, X. Crispin, I. V. Zozoulenko, *Adv. Funct. Mater.* **2017**, *27*, 1700329.
[12] P. Romele, M. Ghittorelli, Z. M. Kovács-Vajna, F. Torricelli, *Nat. Commun.* **2019**, *10*, 3044.
[13] A. Savva, S. Wustoni, S. Inal, *J. Mater. Chem. C* **2018**, *6*, 12023.
[14] I. Zozoulenko, A. Singh, S. K. Singh, V. Gueskine, X. Crispin, M. Berggren, *ACS Appl. Polym. Mater.* **2018**, *1*, 83.
[15] E. Tolstopyatova, N. Pogulaichenko, S. Eliseeva, V. Kondratiev, *Russ. J. Electrochem.* **2009**, *45*, 252.
[16] L. Q. Flagg, R. Giridharagopal, J. Guo, D. S. Ginger, *Chem. Mater.* **2018**, *30*, 5380.
[17] M. Jin, J. Xu, L. Jiang, G. Gao, H. Chu, C. Xiong, H. Gao, P. Jiang, *Electrochemistry* **2014**, *82*, 1040.
[18] a) A. Saydjari, J. P. Long, W. J. Dressick, B. S. Simpkins, *Chem. Phys. Lett.* **2014**, *608*, 328; b) Y. H. Kim, C. Sachse, M. L. Machala, C. May, L. Müller-Meskamp, K. Leo, *Adv. Funct. Mater.* **2011**, *21*, 1076.
[19] C. H. Camp Jr., *J. Res. Natl. Inst. Stand. Technol.* **2019**, *124*, 1.
[20] a) N. Massonnet, A. Carella, O. Jaudouin, P. Rannou, G. Laval, C. Celle, J.-P. Simonato, *J. Mater. Chem. C* **2014**, *2*, 1278; b) J. Hwang, D. Tanner, I. Schwendeman, J. R. Reynolds, *Phys. Rev. B* **2003**, *67*, 115205.
[21] A. Elschner, S. Kirchmeyer, W. Lovenich, U. Merker, K. Reuter, *PEDOT: Principles and Applications of an Intrinsically Conductive Polymer*, CRC Press, Boca Raoton, FL, USA **2010**.
[22] A. Giovannitti, R. B. Rashid, Q. Thiburce, B. D. Paulsen, C. Cendra, K. Thorley, D. Moia, J. T. Mefford, D. Hanifi, D. Weiyuan, M. Moser, A. Salleo, J. Nelson, I. McCulloch, J. Rivnay, *Adv. Mater.* **2020**, *32*, 1908047.
[23] M. Roelfs, P. C. Kroon, tBuLi/symfit: symfit 0.5.3, Zenodo **2020**, https://zenodo.org/record/4020630.
[24] a) J. R. Murdoch, *J. Chem. Educ.* **1981**, *58*, 32; b) P. Atkins, J. D. Paula, *Atkins' Physical Chemistry*, Oxford University Press, Oxford **2006**.
[25] J. H. Espenson, *Chemical Kinetics and Reaction Mechanisms*, Mc Graw-Hill, New York, NY, USA **1981**.
[26] a) S. Arrhenius, *Z. Phys. Chem.* **1889**, *4*, 96; b) H. Eyring, *J. Chem. Phys.* **1935**, *3*, 107.
[27] a) M. Modarresi, J. F. Franco-Gonzalez, I. Zozoulenko, *Phys. Chem. Chem. Phys.* **2019**, *21*, 6699; b) Q. Wei, M. Mukaida, Y. Naitoh, T. Ishida, *Adv. Mater.* **2013**, *25*, 2831; c) S. Rudd, J. F. Franco-Gonzalez, S. Kumar Singh, Z. Ullah Khan, X. Crispin, J. W. Andreasen, I. Zozoulenko, D. Evans, *J. Polym. Sci., Part B: Polym. Phys.* **2018**, *56*, 97.
[28] E. Stavrinidou, P. Leleux, H. Rajaona, D. Khodagholy, J. Rivnay, M. Lindau, S. Sanaur, G. G. Malliaras, *Adv. Mater.* **2013**, *25*, 4488.
[29] E. M. Thomas, M. A. Brady, H. Nakayama, B. C. Popere, R. A. Segalman, M. L. Chabinyc, *Adv. Funct. Mater.* **2018**, *28*, 1803687.
[30] P. C. Hütter, A. Fian, K. Gatterer, B. Stadlober, *ACS Appl. Mater. Interfaces* **2016**, *8*, 14071.
[31] C. M. Proctor, J. Rivnay, G. G. Malliaras, *J. Polym. Sci., Part B: Polym. Phys.* **2016**, *54*, 1433.
[32] K. E. Aasmundtveit, E. J. Samuelsen, O. Inganäs, L. A. A. Pettersson, T. Johansson, S. Ferrer, *Synth. Met.* **2000**, *113*, 93.
[33] Z. Pomerantz, A. Zaban, S. Ghosh, J.-P. Lellouche, G. Garcia-Belmonte, J. Bisquert, *J. Electroanal. Chem.* **2008**, *614*, 49.
[34] a) A. De Juan, J. Jaumot, R. Tauler, *Anal. Methods* **2014**, *6*, 4964; b) A. R. Jalalvand, H. C. Goicoechea, *TrAC, Trends Anal. Chem.* **2017**, *88*, 134.
[35] N. Omidikia, S. Beyramysoltan, J. Mohammad Jafari, E. Tavakkoli, M. Akbari Lakeh, M. Alinaghi, M. Ghaffari, S. Khodadadi Karimvand, R. Rajkó, H. Abdollahi, *J. Chemom.* **2018**, *32*, e2975.